

www.acsnano.org

# Resolving the Nanoscale Structure of $\beta$ -Sheet Peptide Self-Assemblies Using Single-Molecule Orientation-Localization Microscopy

Weiyan Zhou, Conor L. O'Neill, Tianben Ding, Oumeng Zhang, Jai S. Rudra, and Matthew D. Lew\*



Downloaded via WASHINGTON UNIV on April 28, 2024 at 17:33:20 (UTC). See https://pubs.acs.org/sharingguidelines for options on how to legitimately share published articles.

Cite This: ACS Nano 2024, 18, 8798-8810



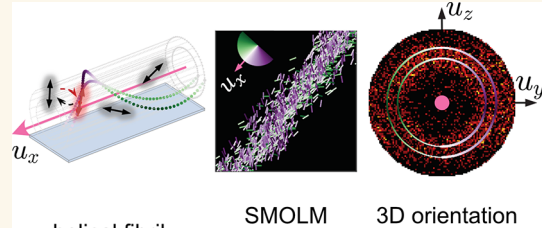
**ACCESS** I

Metrics & More

Article Recommendations

Supporting Information

**ABSTRACT:** Synthetic peptides that self-assemble into cross- $\beta$  fibrils are versatile building blocks for engineered biomaterials due to their modularity and biocompatibility, but their structural and morphological similarities to amyloid species have been a long-standing concern for their translation. Further, their polymorphs are difficult to characterize by using spectroscopic and imaging techniques that rely on ensemble averaging to achieve high resolution. Here, we utilize Nile red (NR), an amyloidophilic fluorogenic probe, and single-molecule orientation-localization microscopy (SMOLM) to characterize fibrils formed by the designed amphipathic enantiomers KFE8<sup>L</sup> and KFE8<sup>D</sup> and the pathological



helical fibril

image

"fingerprint"

amyloid-beta peptide  $A\beta$ 42. Importantly, NR SMOLM reveals the helical (bilayer) ribbon structure of both KFE8 and  $A\beta$ 42 and quantifies the precise tilt of the fibrils' inner and outer backbones in relevant buffer conditions without the need for covalent labeling or sequence mutations. SMOLM also distinguishes polymorphic branched and curved morphologies of KFE8, whose backbones exhibit much more heterogeneity than those of typical straight fibrils. Thus, SMOLM is a powerful tool to interrogate the structural differences and polymorphism between engineered and pathological cross- $\beta$ -rich fibrils.

**KEYWORDS**: self-assembly, supramolecular helix, polymorphism, fluorogenic probes, super-resolution microscopy

eptides that self-assemble into cross- $\beta$  fibrils are an exciting class of biomaterials due to the ease of designing their sequences and their ability to present functional ligands appended to their N- or C-terminus on the fibril surface. In addition to their ability to assemble in aqueous physiological buffers, these structural scaffolds have powerful functionalities for applications in tissue engineering, regenerative medicine, drug delivery, bioorganic semiconductors, and biocatalysis.<sup>2</sup> In peptides with strictly alternating polar and nonpolar residues, e.g., KFE8<sup>3-6</sup> (Ac-FKFEFKFE-NH<sub>2</sub>), hydrophobic and hydrophilic residues are segregated on the opposite sides of the sheet, providing an amphiphilic surface that drives assembly into supramolecular cross- $\beta$ fibrils. However, many cross  $\beta$ -fibrillizing peptide sequences derived from pathological amyloid proteins do not strictly adhere to the alternating polar/nonpolar design, and the role of cross- $\beta$  fibrils in amyloid diseases is a topic of intense study and debate.8 Thus, a wide range of both natural and designed peptide sequences can adopt very similar or even the same cross- $\beta$  structures, and once fibrillized, it can be very difficult to distinguish them based on their morphology.9 Moreover, amphipathic designer peptides assemble into cross- $\beta$ -rich

structures that closely resemble amyloids. 10 Therefore, understanding how toxic, benign, and functional fibrils differ in their molecular packing and nanoscale structure is paramount, but not yet fully understood. Further, the polymorphic nature of amyloid fibrils adds another layer of complexity where a single peptide can form a range of molecularly distinct fibrils.<sup>11</sup>

Existing ultrahigh-resolution characterization tools, e.g., Xray and electron diffraction methods, solid-state NMR spectroscopy, and cryo-EM, 12-16 can achieve atomic resolution but require averaging over an ensemble. Either each polymorphic species must be isolated individually, or extensive data sets must be collected for computational processingboth of which are tremendously challenging. In addition, various sample preparation procedures (e.g., lyophilization and

Received: November 24, 2023 Revised: March 2, 2024 Accepted: March 7, 2024 Published: March 13, 2024





vitrification) can bias assemblies toward specific morphologies. <sup>13</sup> Both atomic force microscopy (AFM) and transmission electron microscopy (TEM) have been widely used for characterizing the morphologies and dimensions of fibrillar peptide assemblies but are blind to the molecular interactions and packing between peptides and the internal structure of self-assembled fibrils. <sup>17</sup>

In the past decade, single-molecule localization microscopy (SMLM) has become a powerful super-resolution fluorescence modality for quantitatively investigating the structural features of amyloids. <sup>17–20</sup> By repeatedly localizing "flashes" from individual fluorophores over time, SMLM has visualized the static and dynamic behavior of self-assembling fibrillar systems and their intermolecular interactions. <sup>21,22</sup> Beyond covalent labeling, binding-activated blinking <sup>23</sup> of environment-sensitive amyloidophilic dyes can also be used for SMLM. Termed transient amyloid binding (TAB), <sup>24</sup> a variety of dyes, including p-TFAA, <sup>25</sup> Nile red (NR), <sup>26–28</sup> thioflavin T, <sup>24</sup> thioflavin X, SYPRO orange, and LDS772, <sup>30</sup> can visualize self-assembling fibrillar systems under physiological conditions for hours to days. However, with localization precisions of ~10 nm, <sup>24,26–29,31</sup> TAB SMLM cannot interrogate nanometer-scale details.

To overcome this limitation, combined imaging of fluorophore positions and orientations,  $^{32}$  termed single-molecule orientation—localization microscopy (SMOLM), has been explored to characterize fibrillar nanostructures with exquisite detail.  $^{26,27,30,33,34}$  Orientation precisions of  $4-8^{\circ}$  are possible when imaging dim emitters ( $\sim$ 500 photons),  $^{27}$  and when using bright fluorophores ( $\sim$ 5000 photons),  $^{20}$  orientation precision in 3D can be achieved.  $^{33}$  Analogous to structural tools like X-ray and electron diffraction, high-precision imaging of fluorophore orientations (angles) yields exquisite nanoscale details of the fibril architecture without the need for nanometer-scale spatial resolution. Unlike these tools, however, SMOLM does not require ensemble averaging to characterize various polymorphs of  $\beta$ -sheet fibril assemblies.

In this study, we utilized SMOLM to visualize nanoscale structural details of cross- $\beta$  fibrils generated from the designer amphipathic sequence KFE8 (Ac-FKFEFKFE-NH<sub>2</sub>) and A $\beta$ 42, a signature of Alzheimer's disease. KFE8 assembles into fibrils with high solubility, and numerous spectroscopic studies have explored the impacts of sequence length and pattern variation on the assembly. Our orientation data reveal that the architectures of both KFE8 and A $\beta$ 42 are consistent with a helical bilayer ribbon, with KFE8 showing clear helicity in its measured backbone tilt angles and A $\beta$ 42 resembling an approximate straight line with modest backbone tilt; these structural features are hidden in standard SMLM. In addition, the rotational "wobble" of NR is significantly smaller and more consistent along the length of A $\beta$ 42 fibrils compared with those of KFE8, thereby demonstrating the exquisite sensitivity of TAB dyes for resolving differences between similar-looking cross- $\beta$  fibrils. SMOLM orientation data also show that KFE8 fibrils exhibit much more structural variability than  $A\beta 42$ fibrils, despite the relative simplicity of the KFE8 sequence. Finally, in addition to typical straight fibrils, SMOLM revealed rare branching, enclosed loop, and curved morphologies of KFE8, all of which were prepared under identical conditions. These unusual morphologies displayed greater heterogeneity and structural diversity, thus demonstrating the power of SMOLM for uncovering and characterizing structural polymorphism.

#### **RESULTS AND DISCUSSION**

Visualizing  $\beta$ -Sheet Assemblies Using Transient Binding-Activated Fluorescent Probes. We performed SMOLM on homochiral KFE8<sup>L</sup>, KFE8<sup>D</sup>, and 42-residue amyloid- $\beta$  peptide (A $\beta$ 42) assemblies using NR (Figure 1a, inset) via the transient binding-activated blinking mechanism (see Experimental Section for details). Due to its solvatochromic and fluorogenic response, 35,36 NR remains dark in water but emits strong fluorescence upon binding to the  $\beta$ -sheet assemblies (Figure 1a). Fluorescence "flashes" from NR coincide with binding and unbinding events, and an ample supply of NR molecules in solution enables a stable rate of blinking NR to be localized along each peptide assembly, whereby even hours-long SMOLM imaging is possible.<sup>24,37</sup> We observe that the number of blinking single molecules (SMs), i.e., localizations, per frame is stable in a typical imaging experiment (Figure S1a), which lasts for 100 s when we capture 5000 frames of each field of view (FOV) (Movie S1). For KFE8<sup>L</sup> and KFE8<sup>D</sup>, 77% of the binding events happen within a single frame (20 ms exposure time); for A $\beta$ 42, 71% of the blinking events occur within 20 ms (Figure S1b).

Without orientation information, standard single-molecule localization microscopy produces nearly indistinguishable images of KFE8  $^{\! \rm L}$  , KFE8  $^{\! \rm D}$  , and A $\beta$ 42 (Figure 1b–d, top, and Figure S2a-c, inset). Visualizing the cross-sectional profiles of KFE8<sup>L</sup>, KFE8<sup>D</sup>, and A $\beta$ 42 fibrils (Figure S2d) produces width measurements of 60-110 nm for KFE8<sup>L</sup> and KFE8<sup>D</sup> and 30-70 nm for A $\beta$ 42 (full width at half-maximum, fwhm, Figure S2e). According to AFM and TEM, KFE8<sup>L</sup> and KFE8<sup>D</sup> have a width of ~8 nm and a pitch of ~20 nm, 5,6,38 while the width and the pitch of A $\beta$ 42 are  $\sim$ 9 nm and  $\sim$ 100 nm, respectively. 39-41 In SMOLM, two factors contribute to the apparent width of the fibrils: (1) localization precision due to Poisson shot noise (11 nm on average for polarized vortex SMOLM, Figure S3) and (2) our TAB imaging strategy; that is, NR may be diffusing near each fibril as it emits fluorescence. Thus, it is almost impossible to reveal the putative ribbon structure and quantify the polymorphs using position information alone, i.e., conventional SMLM.

However, measuring the location and orientation of each blinking fluorophore simultaneously has great potential for revealing supramolecular structural details. Recent SMOLM studies have shown that amyloidophilic dyes like NR bind to  $\beta$ sheet fibrils with their transition dipoles parallel to the fibril backbone (Figure 1a, i), 26,27,42,43 which is consistent with detailed simulation studies of their binding modes. 44-46 If NR molecules bind to grooves along a helical fibril, they will be tilted with respect to the long axis of that fibril (Figure 1a, i). We denote this angle as the backbone tilt angle  $\delta$  (Figure 1a, ii); larger diameter-to-pitch ratios lead to larger backbone tilt angles. Thus, accumulated over the length of the fibril, the orientations of NR measured via SMOLM will form a circle on the orientation sphere, where the  $u_r$  direction is defined to be parallel to the fibril's long axis. Due to dipole symmetry (Figure 1a, ii), the  $u_x < 0$  hemisphere is a replica of the  $u_x \ge 0$ hemisphere. Therefore, only the  $u_x \ge 0$  hemisphere is considered in the following sections.

In this work, SMOLM resolves substantial differences between these  $\beta$ -sheet-formed fibrils, where the location and orientation of each NR molecule are depicted as the center and the direction, respectively, of each line in Figure 1b–d. The lines are color-coded according to the relative angle between

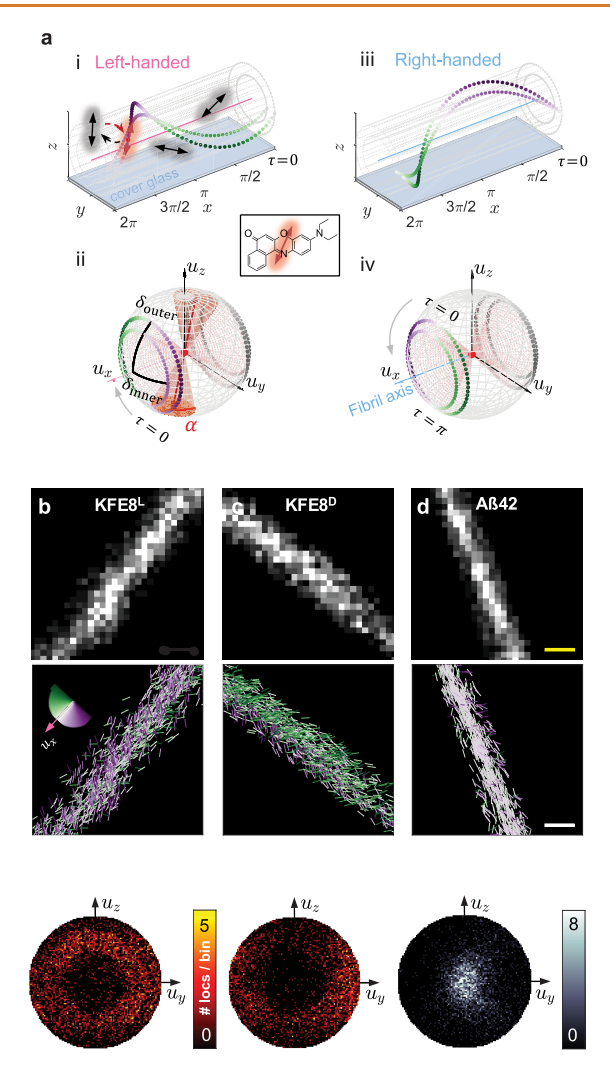


Figure 1. Single-molecule orientation-localization microscopy (SMOLM) of Nile red (NR) reveals the nanoscale structure of the KFE8 and A $\beta$ 42 fibrils. (a) (i) Transient binding of fluorogenic probes (red double-headed arrow) to a left-handed (LH) helical bilayer. Upon binding, the transition dipole moment of NR is parallel to that of the fibrillar backbone, which exhibits a periodic helical twist along its long axis. NR is nonfluorescent in solution (dark arrows). (x, y, z), spatial coordinates defined by the microscope.  $\tau$ , helix phase, which for a helical structure also corresponds to the height of the fibril above the cover glass. Inset: chemical structure of NR. (ii) A model orientation distribution of NR accumulated across all possible binding sites along the helical bilayer  $(u_{x_1}, u_{y_2}, u_{z_3})$ , orientation coordinates defined by the long axis  $u_x$  of the fibril.  $\alpha$ , wobble cone half-angle of NR, quantifying its orientation freedom during a camera frame.  $\delta_{ ext{inner}}$  and  $\delta_{ ext{outer}}$ , inner and outer backbone tilt angles of the helical bilayer, respectively. au= 0 corresponds to a minimum value of  $u_x$  and increases in the direction of the gray arrow. (iii and iv) Right-handed (RH) helical bilayer and the corresponding orientation distribution of NR.  $\tau = 0$ corresponds to a maximum value of  $u_z$  and increases in the direction of the gray arrow. (b-d) (Top) Experimental SMLM images, (middle) SMOLM images, and (bottom) their corresponding 3D orientation distributions on the  $u_x \ge 0$  hemisphere for one typical (b) KFE8<sup>L</sup> (LH), (c) KFE8<sup>D</sup> (RH),  $^{38}$  and (d) A $\beta$ 42 (LH)<sup>39,49</sup> fibril. More examples are shown in Figure S2. Each NR localization is depicted as a line segment whose color and orientation are set by the projection of the molecule's 3D orientation into the xy plane relative to the long axis  $u_x$  of the fibril. Scale bars are 100 nm. The orientation distributions are binned using  $u_v = (-1, -0.98, ..., 1)$  and  $u_z = (-1, -0.98, ..., 1)$ .

the orientation of NR and the long axis  $u_x$  of the fibril. These data are collected by a custom-built polarization-sensitive microscope using a vortex phase mask<sup>27</sup> and analyzed by a bespoke regularized maximum likelihood estimator, RoSE-O<sup>47,48</sup> (see Experimental Section for details).

SMOLM images show that NR molecules bound to KFE8<sup>L</sup> and KFE8D span a large range of orientations (Figure 1b and c, middle), while NR orientations are concentrated near the white region (Figure 1d, middle), i.e., parallel to the fibril axis  $u_{xy}$  for A $\beta$ 42. The distinct structural characteristics of KFE8 and  $A\beta$ 42 are clearly revealed in their corresponding orientation distributions. Both KFE8 systems have a bright ring-like distribution with a dark center (Figure 1b and c, bottom). Conversely, A $\beta$ 42 has a bright center with a dark outer boundary (Figure 1d, bottom). Given the connection between NR orientations and the tilt angle  $\delta$  of the fibril's helical backbone, these data clearly show that the KFE8 fibrils in Figure 1b and c have larger tilt angles  $\delta$  than A $\beta$ 42 does. Therefore, SMOLM reveals the nanoscale details of supramolecular structures and possible polymorphism 18,19,50 beyond what SMLM is capable of. We next quantify how the observed circular orientation distributions are related to the helicity of a supramolecular structure and the number of layers it contains.

**Experimental Characterization of Helical Ribbon Supramolecular Structures Using SMOLM.** The left-handed helical supramolecular structure of KFE8<sup>L</sup> was first observed using AFM and TEM over 20 years ago,<sup>6</sup> and molecular dynamics simulations suggest that the complementary amphipathic β-strands of KFE8 form a bilayer, i.e., a helical ribbon. Since then, the putative helical ribbon model has been widely accepted. Since then, the putative helical ribbon model has been widely accepted. To date, no further direct experimental validation has been realized.

Figure 2a shows the SMOLM orientation distributions of KFE8<sup>L</sup>, KFE8<sup>D</sup>, and  $A\beta$ 42 accumulated from 44 (KFE8<sup>L</sup>), 38 (KFE8<sup>D</sup>), and 32 ( $A\beta$ 42) isolated linear fibrils (example fibrils are shown in Figure 1b–d and Figure S2a–c). Similar to the individual fibrils in Figure 1b–d, we find a bright ring-like distribution with a dim center for KFE8<sup>L</sup> (Figure 2a, left) and KFE8<sup>D</sup> (Figure 2a, middle) and a bright center and a dim boundary in  $A\beta$ 42 (Figure 2a, right).

To determine the supramolecular structure from SMOLM data, we devised a helix optimization algorithm (see Experimental Section), which translates SMOLM orientation measurements into tilt angle estimates (Figure S5a, iii, and iv). Depending on the choice of model, the algorithm finds either (1) a pair of tilt angles ( $\delta_{inner}$ ,  $\delta_{outer}$ ) of a helical bilayer (eq 5) or (2) a single tilt angle  $\delta_{mono}$  (eq 6) that best "fits" the NR orientations observed via SMOLM. To validate model selection and performance of the optimization algorithm, we simulated the process of imaging NR in water binding to helices with specific orientations (Figure S5a, i) using polarized vortex SMOLM (Figure S5a, ii). Briefly, in the case of the helical bilayer model, we treat the pair of measured backbone tilt angles (Figure S5a, iv) as the ground truth. Then, we uniformly sample two circles on the orientation hemisphere that correspond to NR molecules bound to the double-layer helical ribbon. Using vectorial diffraction theory, 54 we simulate images formed by the polarized vortex microscope that are corrupted by Poisson shot noise, and from these images, NR orientations are estimated by RoSE-O.47 The resulting orientation distributions, accumulated over all NR orientations spanning both layers of a helical ribbon, are a realistic

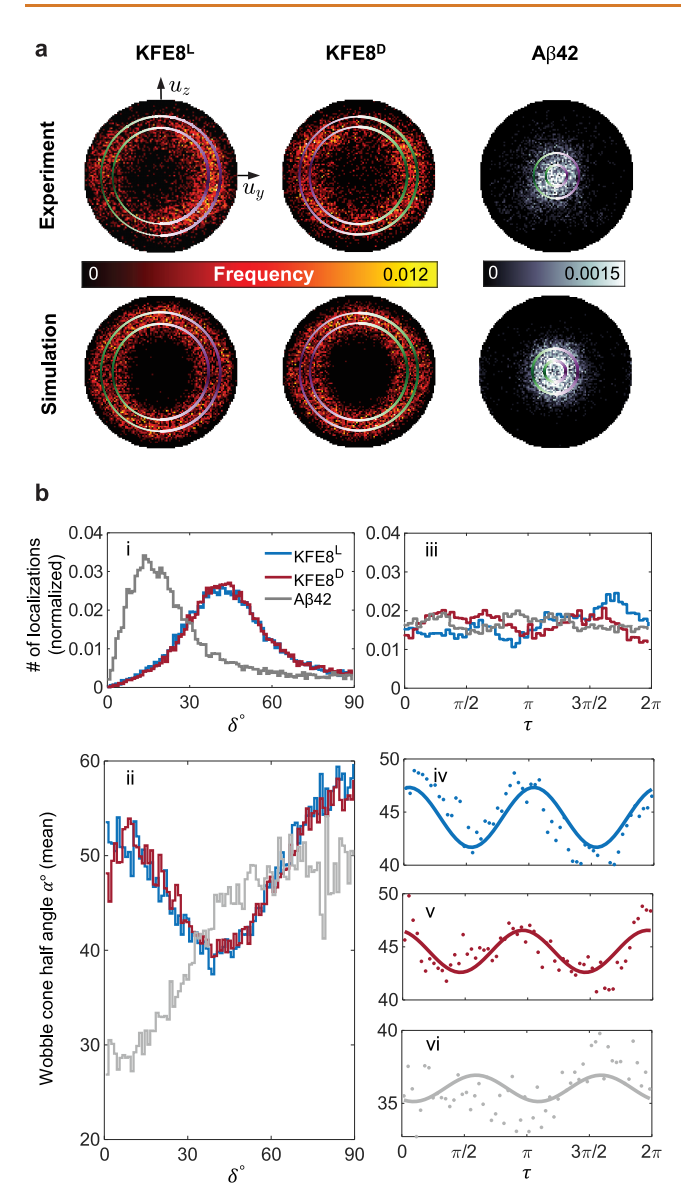


Figure 2. NR orientation distributions, localization densities, and wobble resolve the helical bilayer structures of KFE8 and A $\beta$ 42 fibrils. (a) (top) Experimental and (bottom) simulated orientation distributions of (left) KFE8<sup>L</sup>, (middle) KFE8<sup>D</sup>, and (right) Aβ42 with overlaid backbone tilt angles  $\delta_{ ext{inner}}$  and  $\delta_{ ext{outer}}$  calculated using our helix optimization algorithm (see Figure S5). The circles, i.e., the measured backbone tilt angles, are color-coded with respect to helix phase  $\tau$  (see Figure 1a). The orientation distributions are binned using  $u_y = (-1, -0.98, ..., 1)$  and  $u_z = (-1, -0.98, ..., 1)$ . Filter: signal  $\geq$  500 photons, webble cone half angle  $\alpha \leq 30^{\circ}$ . (b) NR (i, iii) localization density and (ii, iv-vi) wobble quantified as a half-cone angle  $\alpha$  in degrees. Filter: signal  $\geq$  500 photons. (i, ii) Localization density and wobble are quantified with respect to backbone tilt angle  $\delta$ . Bin size: 1°. (iii–vi) Localization density and wobble are quantified with respect to helix phase  $\tau$ . (iv-vi) SMOLM measurements are represented as points; solid lines are from fits to sinusoidal functions. Bin size:  $\pi/30$  (6°). Data are accumulated from all measured fibrils. See Figures \$10 and \$11 for full distributions.

simulation of SMOLM imaging of a helical ribbon with known backbone tilt angles.

We performed extensive simulations to validate the robustness of our helix optimization strategy. First, we

simulated 20 helical ribbons with backbone tilt angles similar to those of KFE8 and found that the algorithm has high accuracy and precision (Table S1, 5040 SMs per ribbon matching our experiments). The bias in measuring backbone tilt is less than 1° and 1.5° in 87.5% and 97.5% of the cases, respectively, while our precision in estimating both  $\delta_{\mathrm{inner}}$  and  $\delta_{
m outer}$  is less than 1.1°. Second, we found that the algorithm is robust against the number of SMs (Figure S7a). The standard deviation is less than 0.5°, and the bias is less than 0.65° even when the number of SMs is only around 300. When the number of SMs reaches 5000, the standard deviation reduces to 0.2°, and the bias is 0.59°. Third, to investigate the generality of SMOLM's ability to measure helical structures, we simulated monolayer helices with backbone tilt angles  $\delta$ ranging from  $0^{\circ}$  to  $90^{\circ}$  (Figure S7b). When  $\delta \in [10^{\circ}, 80^{\circ}]$ , the helix optimization algorithm shows a bias less than 1.1°, with precision less than 0.1° (630 SMs per helix, 10 helices with the same size for precision quantification). For helices with a 20 nm pitch,  $\delta = 10^{\circ}$  corresponds to a radius of 0.56 nm and  $\delta =$  $80^{\circ}$  to 18.05 nm. We found that the bias is monotonic outside this range and can be corrected using these data to restore accuracy. Due to computational cost, we did not quantify the performance of measuring  $\delta_{\text{inner}}$  and  $\delta_{\text{outer}}$  for helical ribbons across the entire range, 0° to 90°. Overall, our simulations of SMOLM and its associated orientation analysis show excellent performance for helical structure determination.

Using our algorithm, we found that the backbone tilt angles of the inner and the outer layers of KFE8<sup>L</sup> are  $\delta_{inner} = 38.90^{\circ}$ and  $\delta_{\text{outer}} = 50.34^{\circ}$  (Figure 2a, top left, 5194 total SMs). Assuming a pitch of 20 nm,  $^{5,6,38}$  the corresponding radii of the inner and outer layer are 2.57 and 3.84 nm, respectively. The backbone tilt angles of KFE8<sup>D</sup> are  $\delta_{\rm inner}$  = 39.20° and  $\delta_{\rm outer}$  = 50.58° (Figure 2a, top middle, 5104 total SMs), corresponding to inner and outer layer radii of 2.60 and 3.87 nm, respectively. These measurements are consistent with TEM.<sup>38</sup> In contrast, the tilt angles of the inner and outer layers of A $\beta$ 42 are  $\delta_{inner}$  = 7.86° and  $\delta_{\text{outer}} = 16.96^{\circ}$  (Figure 2a, top right, 4646 total SMs). The experimental NR orientation distributions (Figure 2a, top) match our simulated orientation distributions of a helical ribbon (Figure 2a, bottom) for both KFE8 and A $\beta$ 42. On the other hand, simulated orientation distributions of a helical monolayer (Figure S6c) are much narrower than the experimental distribution even when accounting for noise stemming from photon counting and a finite number of NR localizations. Therefore, SMOLM shows that NR binds to these  $\beta$ -sheet fibrils in a manner consistent with double-layer ribbons instead of single-layer tapes.

Structural Insights of  $\beta$ -Sheet Assemblies Revealed by Fluorogenic Probes. Since NR molecules emit fluorescence only when bound to each fibril, we posited that the photophysical and rotational behavior of each NR molecule could reveal insights into the structure of each  $\beta$ -sheet assembly. Thus, we quantified the localization density and the "wobble" cone half-angle  $\alpha$  (Figure 1a, ii) of the SMs as a function of backbone tilt angle  $\delta$ . We note that our helical model features a one-to-one mapping between backbone tilt angle (eqs 2 and 4) and molecule position (eqs 1 and 3) relative to the fibril's central axis. Thus, for a given fibril, a NR molecule with relatively small  $\delta$  may be interpreted as binding to an "interior" binding site close to the central axis, while large  $\delta$  values correspond to "exterior" sites that are relatively far from the axis (Figure 1a, pink and blue axes).

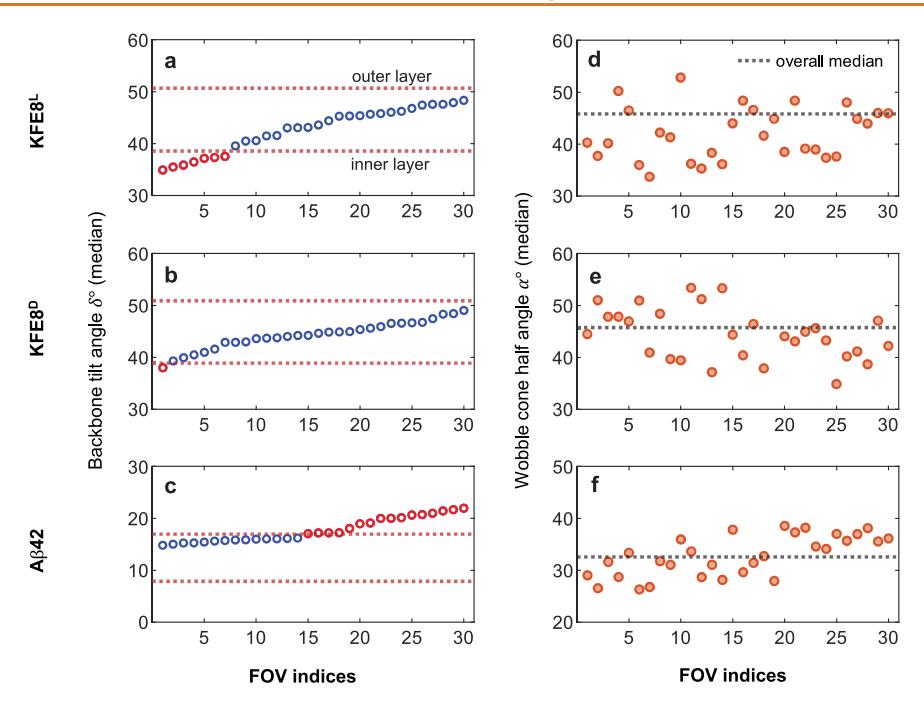


Figure 3. NR SMOLM quantifies the heterogeneity among KFE8<sup>L</sup>, KFE8<sup>D</sup>, and  $A\beta$ 42 fibrils. (a–c) Median backbone tilt angles  $\delta$  of NR measured within 30 fields of view (FOVs) for (a) KFE8<sup>L</sup>, (b) KFE8<sup>D</sup>, and (c)  $A\beta$ 42. Hollow circles are median angles within each FOV. Red dotted lines are the backbone tilt angles  $\delta$ <sub>inner</sub> and  $\delta$ <sub>outer</sub> of KFE8<sup>L</sup>, KFE8<sup>D</sup>, and  $A\beta$ 42, as estimated by the helical optimization of data accumulated across all FOVs shown in Figure 2a. (d–f) Median wobble cone half-angles  $\alpha$  measured within 30 FOVs for (d) KFE8<sup>L</sup>, (e) KFE8<sup>D</sup>, and (f)  $A\beta$ 42. Orange circles are the median angles within each FOV. Black dotted lines are median angles over all KFE8<sup>L</sup>, KFE8<sup>D</sup>, and  $A\beta$ 42 FOVs in Figure 2b. KFE8<sup>L</sup> FOV 26 corresponds to the fibril shown in Figure 1b; FOV 4 to Figure S2a, i; FOV 16 to Figure S2a, ii; FOV 12 to Figure S2a, iii; and FOV 21 to Figure S2a, iv. KFE8<sup>D</sup> FOV 30 corresponds to the fibril shown in Figure 1c; FOV 22 to Figure S2b, i; FOV 15 to Figure S2b, ii; FOV 18 to Figure S2b, iii; and FOV 7 to Figure S2b, iv.  $A\beta$ 42 FOV 7 corresponds to the fibril shown in Figure 1d; FOV 29 to Figure S2c, ii; FOV 19 to Figure S2c, iii; and FOV 10 to Figure S2c, iv.

Enantiomeric KFE8<sup>L</sup> and KFE8<sup>D</sup> feature almost identical localization density curves (Figure 2b, i, KFE8<sup>L</sup>: 24715 total localizations, KFE8<sup>D</sup>: 25 283 total localizations, A $\beta$ 42: 15 708 total localizations), which means that NR binds similarly to KFE8<sup>L</sup> and KFE8<sup>D</sup> even though they have opposite handedness. We find 38% and 37% of binding events correspond to the interior of KFE8<sup>L</sup> ( $\delta \leq 38.90^{\circ}$ ) and KFE8<sup>D</sup> ( $\delta \leq 39.20^{\circ}$ ), respectively, while 29% and 30% of the SMs visited the region between the two layers of KFE8<sup>L</sup> (38.90°  $< \delta < 50.34$ °) and KFE8<sup>D</sup> (39.20° <  $\delta$  < 50.58°), respectively. The rest (33% for both KFE8<sup>L</sup> and KFE8<sup>D</sup>) exhibited tilt angles consistent with the exterior of the ribbon (KFE8<sup>L</sup>:  $\delta \geq 50.34^{\circ}$  and KFE8<sup>D</sup>:  $\delta \geq$ 50.58°). In contrast, NR gives a distinctly different localization density distribution when binding to A $\beta$ 42 fibrils. We observed 10%, 27%, and 63% of the localizations to be within the inner layer ( $\delta \leq 7.86^{\circ}$ ), within the bilayer ( $7.86^{\circ} < \delta < 16.96^{\circ}$ ), and from the outer layer ( $\delta \geq 16.96^{\circ}$ ), respectively. The peak localization densities correspond to backbone tilt angles of 41° for KFE8<sup>L</sup>, 44° for KFE8<sup>D</sup>, and 13° for A $\beta$ 42. The larger angles  $\delta$  for homochiral KFE8 imply that they have a larger diameterto-pitch ratio than A $\beta$ 42, which is consistent with previous studies of KFE8<sup>6,38,51,52</sup> and A $\beta$ 42.<sup>39–41,55</sup>

We next examine the "wobble" of NR while bound to each fibril, quantified as a half-cone angle  $\alpha$  explored by NR during a camera frame (Figure 1a, ii). We find considerable similarity between the enantiomeric KFE8 pairs (Figure 2b, ii), suggesting that opposite handedness does not significantly affect the local binding behavior of NR to each assembly. NR shows a minimum wobble when  $\delta \in [38^{\circ}, 50^{\circ}]$ , which corresponds to the region between the two layers of the helical

ribbon. Notably, this trend is in good agreement with the helical ribbon model of KFE8, in which the phenylalanine residues are buried inside to form a hydrophobic core. NR exhibits stronger and more frequent binding in this hydrophobic core versus the more polar exterior, and SMOLM consequently detects a greater number of NR molecules within this range of tilt angles with a commensurate minimum in rotational freedom. In stark contrast for A $\beta$ 42 (Figure 2b, ii), NR demonstrates systematically larger wobble for larger tilt angles, which correspond to binding to the helix exterior. When  $\delta \leq 16.96^{\circ}$ , i.e., inside the inner layer and between the bilayer, the wobble angle of NR is at a nearly stable minimum near 30°. This small rotational freedom implies that the sidechain grooves of A $\beta$ 42 fibrils more strongly constrain the rotation of NR than those of KFE8 systems, thereby demonstrating the potential of SMOLM for sensing the structure and chemical environments of  $\beta$ -sheet assemblies.

Interestingly, for both KFE8 and  $A\beta$ 42, we find that the localization density of NR reaches a maximum (Figure 2b, i) at nearly the same backbone tilt angles as where the wobble of NR attains its minimum (Figure 2b, ii). Specifically, NR with orientations further from the most frequently measured backbone tilt angles ( $\delta \in [38^{\circ}, 50^{\circ}]$  for KFE8 and  $\delta \in [8^{\circ}, 17^{\circ}]$  for  $A\beta$ 42) exhibit larger wobbles than those whose tilt angles lie near the peak. We interpret this correlation to be consistent with the TAB blinking mechanism of NR (Figure 1a); when NR molecules are farther away from the assemblies, they have more rotational freedom. In addition, the surrounding chemical environment is more polar, leading to a smaller quantum yield and fewer SM localizations. Thus, for

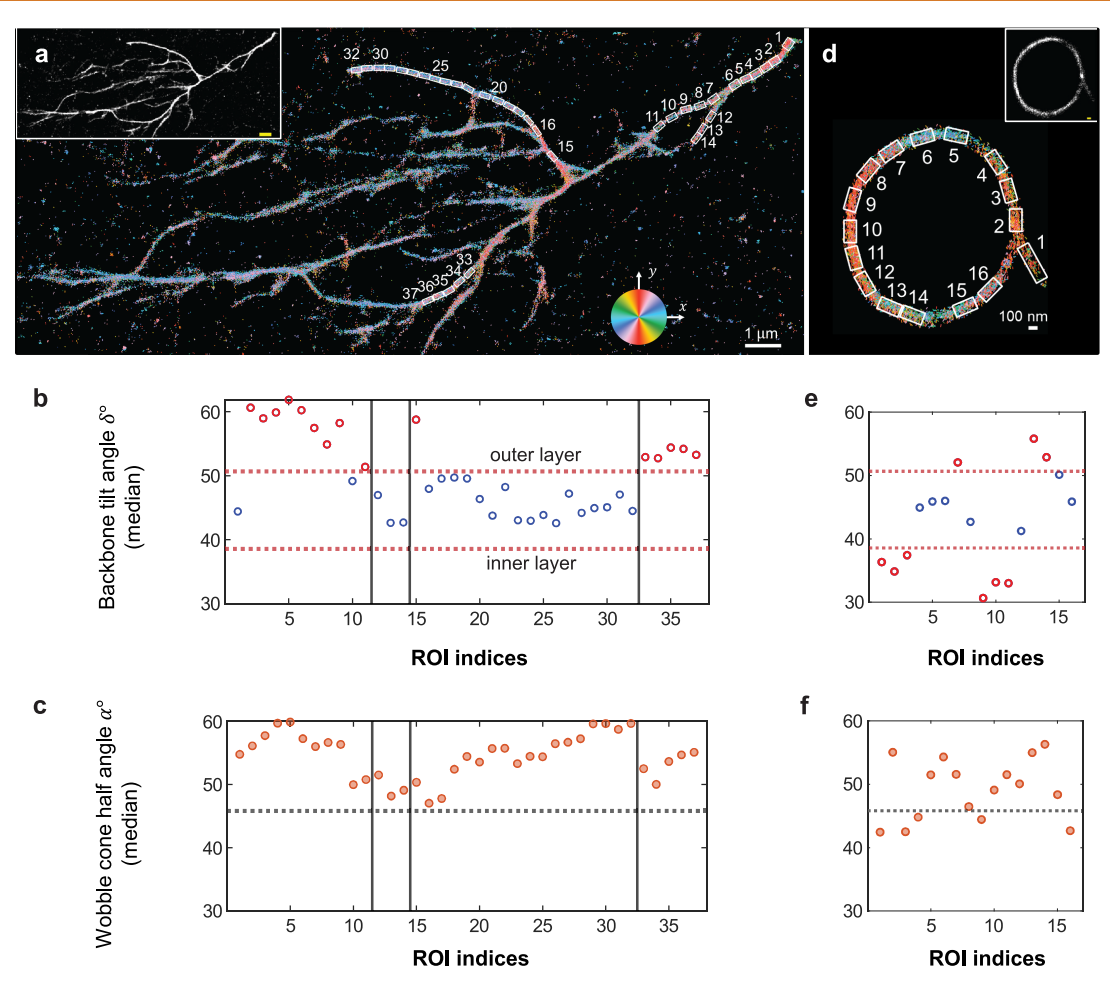


Figure 4. Structural polymorphism of KFE8<sup>L</sup> revealed by SMOLM: (a-c) Branching and (d-f) enclosed loop structures. In (a)-(c), two "parent" branches (ROIs 1-6 and 15-32) and three "child" branches (ROIs 7-11, 12-14, and 33-37) are chosen. (a and d) SMOLM and (inset) SMLM images. NR orientations in the SMOLM images are represented as colored disks in (a) (108 038 localizations [59% of the data] are randomly selected for plotting in (a) to avoid oversaturation) and colored lines in (d) (all data are shown). Each disk/line is color-coded according to the projection of the 3D NR orientation into the xy plane relative to the  $\mu_x$  axis, which is defined by the microscope instead of the long axis of the fibril. (b and e) Median backbone tilt angles  $\delta$  within each region of interest (ROI), which are shown in SMOLM images. Red dotted lines are the backbone tilt angles of the helical bilayer, as estimated by helical optimization of data accumulated across all FOVs shown in Figure 2a, left. Blue circles lie within the estimated backbone tilt angles of the bilayer; red circles outside the range. (c and f) Median wobble angle  $\alpha$  (orange circles) within each ROI. Black dotted lines are the median of the accumulated experimental data in Figure 2b. For more examples, see Figure S14. Scale bars: (a and inset) 1  $\mu$ m, (d and inset) 100 nm.

 $\beta$ -sheet assemblies, smaller NR wobble is likely directly linked to more hydrophobic binding sites, which in turn yield more frequent NR localizations.

We next characterize NR localization density and rotational freedom along the helices, parametrized by phase  $\tau$  (with  $\tau \in$  $[0, 2\pi)$  defined as in Figure 1a, i–iv). We find that NR binds with a near-uniform frequency along each fibril, regardless of the variant (Figure 2b, iii). Surprisingly, however, we find striking sinusoidal variations in the half cone angle  $\alpha$  as a function of helix phase  $\tau$  (Figure 2b, iv–vi), i.e., as the fibrils rise and fall with respect to the coverslip (Figure 1a, ii, and iv). Fitting the wobble angle measurements to sinusoid functions yields  $\alpha_L = 2.8^{\circ} \cos(2\tau - 0.25) + 44.5^{\circ}$  for KFE8<sup>L</sup>,  $\alpha_D = 2.0^{\circ}$  $\cos(2\tau + 0.24) + 44.6^{\circ}$  for KFE8<sup>D</sup>, and  $\alpha_{A\beta42} = -0.9^{\circ} \cos(2\tau - 0.00)$ 0.58) + 36.0°; we constrain the frequency of each sinusoid to ensure continuity over  $\tau$ . These variations for KFE8 are significantly larger, by more than two times, than what can be expected from shot noise alone (see simulations in Figure S8a where  $\alpha$  is held constant). Further, there are no correlations

between measurement errors in  $\alpha$  versus errors in location and mean orientation (Figure S9).

Notice that the wobble angle  $\alpha$  oscillates twice over a single helical period for KFE8<sup>L</sup> and KFE8<sup>D</sup> (Figure 2b, iv-vi), achieving minima near  $\tau = \pi/2$  and  $\tau = 3\pi/2$  (Figure 2b, iv and v); this minimum wobble occurs where the helices are either in contact with the glass coverslip or are furthest away from the coverslip. In addition, we observe that the average wobble of NR is almost the same when binding to KFE8<sup>L</sup> and KFE8<sup>D</sup>, but the variations in the wobble along the helix are 40% larger for KFE8<sup>L</sup> than for KFE8<sup>D</sup>. In contrast, NR exhibits a different wobble behavior when bound to A $\beta$ 42 (Figure 2b, vi). As opposed to reaching minima as in KFE8, NR rotational freedom is maximized for sections of A $\beta$ 42 fibrils that are close to and far away from the cover glass, albeit with variations that are approximately half as large for A $\beta$ 42 compared to KFE8. One possible reason for this difference is A $\beta$ 42's relatively smaller backbone tilt angles (Figure 2a, top), which means that its fibrils more closely resemble straight lines instead of helices; we may expect periodic variations to be less significant for

structures with less helical character. We also note that the wobble angles  $\alpha$  of A $\beta$ 42 fibrils along  $\tau$  deviate more strongly from the sinusoidal fit, which again stems from the smaller backbone tilts of A $\beta$ 42. Since the helix phase is calculated from the orientation ( $u_y$ ,  $u_z$ ) of each localized molecule (eq 2), we expect greater uncertainty in calculating  $\tau$  for fibrils exhibiting smaller  $\delta$ , even if the orientation measurement precision is held constant.

Nile Red Orientations Reveal Polymorphism across Fibrils of KFE8 and A $\beta$ 42. Characterizing polymorphism of self-assembling peptides is critical to the rational design of biomaterials<sup>9,56</sup> and effective drug-delivery vehicles.<sup>57,58</sup> Polymorphism has been studied in both synthetic and natural systems, 4,59,60 but structure—function relationships remain difficult to characterize due to methodological challenges. Motivated to unmask possible polymorphism, we quantified backbone tilt angles  $\delta$  and wobble cone half-angles  $\alpha$  of NR bound to linear and isolated fibrils of KFE8<sup>L</sup>, KFE8<sup>D</sup>, and A $\beta$ 42 across 30 FOVs for each peptide. Representative SMOLM images are shown in Figure 1b-d and Figure S2ac. Sorting the FOVs according to the median backbone tilt angle, we observe considerable variations in measured backbone tilts of KFE8 (Figure 3a and b) that are hidden when data are averaged across all fibrils (Figure 2). The medians of the backbone tilt angle  $\delta$  within each FOV range from 35° to 48° for KFE8<sup>L</sup> (Figure 3a), 38° to 49° for KFE8<sup>D</sup> (Figure 3b), and  $15^{\circ}$  to  $22^{\circ}$  for A $\beta$ 42 (Figure 3c). Surprisingly, despite its short sequence, the fibrils of KFE8 display much more structural variability than those of A $\beta$ 42 in our experiments.

We also observe a large variation in NR wobble across FOVs (Figure 3d–f; for full distribution, see Figure S12). The overall median wobble is  $46^{\circ}$  for both KFE8<sup>L</sup> and KFE8<sup>D</sup> (Figure 3d and e). However, NR wobble on each fibril tends to be more constrained, with 70% of the KFE8<sup>L</sup> FOVs (Figure 3d) and 63.33% of the KFE8<sup>D</sup> FOVs (Figure 3e) having a median smaller than that of the accumulated localizations. The analogous statistics for  $A\beta$ 42 are more symmetric, with an overall median of 33° (Figure 3f) and 53.33% of the FOVs having a median larger than that of the accumulated FOVs (Figure 2b, vi).

In aqueous media, we observed not only linear fibrils but also rare KFE8 morphologies, including branching (Figure 4a) and enclosed (Figure 4d) structures (see Figure S14 for more examples). Recently, branching has also been observed using high-speed atomic force microscopy,<sup>3</sup> but to our knowledge, enclosed, looping structures have never been reported. SMOLM images (Figure 4a and d) depict NR orientations projected into the *xy* plane, which show striking diversity when bound to the underlying supramolecular helices. These detailed variations in structure are impossible to detect using other techniques.

To investigate these polymorphs more closely, we analyzed individual segments along each structure, each with a length of 250 nm except for ROI 1 in Figure 4d, which was lengthened to 400 nm to ensure sufficient localization statistics. We found notable systematic deviations from the behavior of typical fibrils. First, the *median* backbone tilt angles  $\delta$  of one parent branch (ROIs 1–11, Figure 4b) are around 6° larger than the tilt  $\delta_{\text{outer}} = 50.34^{\circ}$  of the *outer layer* of typical KFE8<sup>L</sup> fibrils (Figure 3a). However, this trend does not hold for an offshoot child branch (ROIs of 12–14). Another parent branch (ROIs 15–32) is comparable to typical assemblies, with median  $\delta$ 

angles that are between  $\delta_{\rm inner}$  and  $\delta_{\rm outer}$ . Second, we found that all measured NR wobble angles for the branching structure (Figure 4c) are larger than those of linear fibrils. Thus, this branching KFE8 morphology contains binding sites that allow NR to rotate more freely, even while bound, than typical linear fibrils do.

We also find that the enclosed ring morphology of KFE8<sup>L</sup> fluctuates along its circumference (Figure 4e). Of the 16 regions we analyzed, six of them show median backbone tilt angles that are smaller than the tilt  $\delta_{inner}$  of the inner layer of typical linear fibrils (Figure 3a). These data imply that locally these fibril segments have smaller diameters or longer periodicity than typical ones. Interestingly, three ROIs have larger tilt angles  $\delta$  than *every* straight fibril we observed (Figure 3a). We also observed varying degrees of NR rotational wobble along the entire structure (Figure 4f), with 69% of the segments exhibiting a median  $\alpha$  larger than that of typical linear fibrils. Analyses of similar enclosed and curved fibrils of KFE8<sup>D</sup> reveal similar behaviors (Figure S14); local segments show heterogeneous backbone tilts  $\delta$  and rotational wobble  $\alpha$ , some of which deviate from typical observations (Figure 3b). Overall, SMOLM analysis shows that the morphologies of KFE8 assemblies exhibit strong variations, both between and within individual fibrils. Moreover, unusual morphologies, such as branching, looped, and curved structures, show more heterogeneity than linear segments do.

#### CONCLUSION

Peptides that self-assemble into cross  $\beta$ -sheet fibrils have broad relevance across seemingly unrelated fields.<sup>2,61</sup> To gain molecular and structural insights into misfolded states of proteins involved in neurodegenerative diseases, scientists developed minimal peptide fragments<sup>62–65</sup> capable of emulating the behavior of the parent protein and demonstrated that small peptides can self-assemble into supramolecular structures. They also provided a deeper understanding of the formation of oligomeric intermediates and disease pathogenesis. Independently, a second family of designer peptides composed of amphipathic sequences with strictly alternating hydrophobic and charged residues were first identified in Saccharomyces cerevisiae. 66 This class of peptides also assemble into cross- $\beta$ -sheet fibrils and have attracted considerable interest as biomaterial scaffolds due to their ability to form hydrogels.<sup>67</sup> The close resemblance of these various cross-βrich structures directly contrasts with their disparate sequences and differing toxicity and function; the connections among molecular packing, structure, and biological functions are not yet fully understood.

The polymorphic nature of amyloid fibrils adds another layer of complexity, where a single peptide can form a range of molecularly distinct fibrils.  $^{4,11,68,69}$  Structural polymorphs consistently manifest themselves as subtle alterations in the morphology and structure of  $\beta$ -sheet assemblies, arising from differences in inter- or intraresidue interactions, the number of amino acid residues, their packing, and their orientations. Computational and spectroscopic studies confirm that structural variations in pathological amyloid fibrils can be responsible for the observed disease variations in multiple neuropathies.  $^{70}$  A $\beta$  fibrils formed *in vitro* are especially polymorphic, with a range of conformations that vary with the conditions of their preparation.  $^{71-74}$  Interestingly, cryoelectron microscopy of KFE8 recently identified the presence of multiple polymorphic species assembled under various

conditions.<sup>5</sup> Whereas sequence variation of amphipathic peptides has been exploited to control long-range and bulk material properties, such as crystallinity, gelation, morphology, and mechanical properties, reliable prediction of the supramolecular structure from sequence information remains a significant challenge. Characterizing polymorphism is thus critical to elucidating structure—function relationships as well as accelerating the rational design of functional biomaterials.

Conventional bulk analysis and ensemble-based measurements may mask structural heterogeneity between and within individual fibrils and, therefore, be blind to rare species. In this work, we use NR TAB to noncovalently label KFE8 and A $\beta$ 42, thereby enabling SMOLM to characterize individual  $\beta$ -sheet fibrils with single-molecule sensitivity. NR orientation distributions accumulated across a multitude of isolated straight fibrils are consistent with a helical bilayer ribbon model (Figure 2), and a bespoke helix optimization algorithm measures the associated backbone tilt angles  $\delta_{\mathrm{inner}}$  and  $\delta_{\mathrm{outer}}$ with excellent precision and accuracy (Figures S6 and S7 and Table S1). The larger degree of polymorphism in KFE8 versus  $A\beta 42$  is obvious when comparing the median backbone tilt angle and wobble of the NR in each field of view individually. This extensive variation (Figure 3) is otherwise hidden by ensemble-averaged measurements (Figure 2). Finally, our analysis of branching, enclosed looping, and curved morphologies of KFE8 shows that their fibrils are distinct (Figures 4 and S14) from those of straight fibrils, thereby providing a first link between nanoscale helical ribbons and micron-scale morphology. Almost universally, we found significant variations both within and between individual fibrils, thereby underscoring the necessity of characterizing these structures in aqueous media with the single-fibril sensitivity and nanoscale resolution afforded by TAB SMOLM.

We note that the structural details in our study are powerfully conveyed by the connection between a supramolecular structure and the orientations of its binding sites for amyloidophilic probes (Figure 1a). While the binding orientations of NR to A $\beta$ 42 fibrils are consistent with a double-layer ribbon model (Figure S6), we can also interpret these data as two types of binding sites that are linked to two different backbone tilt angles. Since high-resolution ssNMR and cryo-EM show S-shaped conformations formed by the stacking of A $\beta$ 42 peptides, we hypothesize that the backbone tilts  $\delta_{\text{inner}}$  and  $\delta_{\text{outer}}$  measured by SMOLM correspond to two helical grooves within A $\beta$ 42 fibrils. Further theoretical and experimental investigations are necessary to determine the precise binding behaviors of the NR.

As such, it is important to expand the library of TAB-compatible fluorophores<sup>29,30</sup> both to probe dye—structure interactions and to broaden the applicability of TAB SMOLM to various classes of peptide assemblies. Even using existing probes, our imaging strategy should be readily adaptable to helices of different radii, periodicity, peptide sequences, and chirality. Fundamentally, SMOLM enables high-fidelity structural characterization via precise measurements of molecular orientation, rather than via ångström-level spatial resolution, but we note that SMOLM orientation data ideally complement traditional spatial imaging. For example, if two targets of interest produce nearly identical orientation distributions (e.g., KFE8<sup>L</sup> and KFE8<sup>D</sup> in Figure 2) and contain similar densities of hydrophobic binding sites for TAB probes,<sup>31</sup> then subnanometer imaging resolution<sup>75,76</sup> will be critical for resolving structural variations.

Our demonstration establishes SMOLM's capability for future experimental structure-function studies of self-assembling peptides in native conditions without mutating or permanently modifying the peptides themselves. We note that the origin and implications of the sinusoidal variation in NR wobble along fibrils of KFE8 and A $\beta$ 42 (Figure 2b iv–vi) are still open questions. We hypothesize that the accessibility of binding sites and the chemical environment along each fiber are correlated with the direction  $(u_x, u_y)$  and  $u_z$  of the fibrillar backbone, at least for fibrils adsorbed to glass. Since NR only emits fluorescence in sufficiently hydrophobic environments, our wobble measurements could be signatures of architectural variations within each helical structure. Further experimental characterization and theoretical studies of how fluorophore wobble is related to supramolecular structure will be helpful. These future developments will enable detailed investigation of polymorphic structures and their impact on the design and function of next-generation biomaterials. 77,78

## **EXPERIMENTAL SECTION**

Sample Preparation and Imaging Using Polarized Vortex SMOLM. KFE8<sup>L</sup> (Ac-FKFEFKFE-NH2) and KFE8<sup>D</sup> (Ac-fkfefkfe-NH2) peptides were synthesized using standard 9-fluorenylmethoxyearbonyl (Fmoc) chemistry and purified as detailed in our previous publication.<sup>38</sup> To prepare a KFE8 stock solution for TAB imaging, we dissolved lyophilized KFE8 directly into ultrapure water to a concentration of 0.2 mM at room temperature. A $\beta$ 42 peptide (DAEFRHDSGYEVHHQKLVFFAEDVGSNKGAIIGLMVGGVVIA) was synthesized and purified by James I. Elliott (ERI Amyloid Laboratory, Oxford, CT, USA). An A $\beta$ 42 stock solution was prepared for imaging as described previously. 26,27 Briefly, we suspended the purified amyloid powder in hexafluoro-2-propanol (HFIP) and sonicated it at room temperature for 1 h. Then, the solution was lyophilized. Next, we further purified the amyloid precursors by dissolving the lyophilized A $\beta$ 42 in 10 mM NaOH, followed by a 25 min cold water bath. The solution was filtered through a 0.22  $\mu$ m and 30 kDa centrifugal membrane filter (Millipore Sigma, UFC30GV and UFC5030). The amyloid fibrils were prepared by incubating 10  $\mu$ M monomeric A $\beta$ 42 in phosphate-buffered saline (150 mM NaCl, 50 mM Na<sub>3</sub>PO<sub>4</sub>, pH 7.4) at 37 °C with 200 rpm agitation for 24 h. We found the stock KFE8 and A $\beta$ 42 solutions to be stable at 4  $^{\circ}$ C over 1 week, similar to previous reports. 17,79 All imaging experiments were completed within 1 week of preparing these stock solutions.

For SMOLM experiments, the KFE8 solution was further diluted to 2  $\mu$ M with ultrapure water to observe the isolated fibrils. We diluted A $\beta$ 42 to a concentration of 10  $\mu$ M in ultrapure water for imaging of individual fibrils. For imaging, 10  $\mu$ L of the solution containing  $\beta$ -sheet assemblies was added to an ozone-cleaned eightwell chambered cover glass (high-tolerance No. 1.5, Cellvis, C8-1.5H-N) and set aside for 1 h to allow fibrils to adsorb to the glass. Afterward, we gently rinsed it using ultrapure water for less than 10 s before drying. Next, 200  $\mu$ L of a solution containing 25 nM Nile red (Fisher Scientific, AC415711000) in ultrapure water was added gently for imaging.

Imaging experiments were performed using our custom-built epifluorescence microscope equipped with the polarized vortex dipole-spread function (DSF). A circularly polarized 532 nm laser (~0.73 kW/cm² peak intensity) was used to illuminate the sample at normal incidence. A 1.4 NA oil-immersion objective lens (Olympus UPlan-SApo 100×), dichroic beamsplitter (Chroma, ZT532/640rpc-UF1), and bandpass filter (Semrock, FF01-593/46) were used to collect and isolate fluorescence from NR within the emission path of the microscope. Polarization-sensitive fluorescence detection using the vortex DSF was implemented using a 4f optical system, polarizing beamsplitter (PBS), and liquid-crystal spatial light modulator (SLM, Meadowlark, HSPDM256-520-700-P8) as previously described. Briefly, after the first 4f lens, a PBS splits fluorescence into two orthogonally polarized light paths, and the SLM is placed at the

coaligned conjugate back focal plane of both polarization channels. The vortex phase mask is loaded onto the SLM to modulate the NR fluorescence. Finally, the second 4f lens in each channel creates nonoverlapping images of the two polarization channels on a single sCMOS camera (Teledyne Photometrics, Prime BSI). For each FOV, we captured at least 5000 frames with a 20 ms exposure time.

Polarized Vortex SMOLM Image Analysis. The raw images collected by the detector were first converted from AD counts to detected photons by subtracting the camera offset and multiplying by the camera's conversion gain. Second, the fluorescence background within the raw images was estimated exactly as described previously. Briefly, the raw image stacks were separated into 200-frame substacks, and one averaged image was calculated from each substack. Each row and column of the averaged images were fitted to the sum of two 1D Gaussian functions, which in total contain six parameters, including two amplitudes, two centers, and two standard deviations. The averages of the rowwise and columnwise Gaussian fits were used for spatial filtering, which was realized by a biorthogonal wavelet filter (wavedec2 and wdencmp functions in Matlab with parameter level 6 of bior6.8').

Third, we performed image registration between the two orthogonally polarized channels of our microscope. To determine the geometric relationship between the two channels, we captured images of sparse fluorescent beads (Thermo Fisher Scientific, FluoSphere, 540/560, F8800) that are spin-coated on an ozone-cleaned cover glass. The localizations of the beads were determined using the ThunderSTORM plugin within ImageJ. Localizations of the same bead from multiple consecutive frames were averaged to improve the localization precision. Corresponding control point pairs of each bead across the two channels were used to determine the registration map, which is composed of the coefficients of a 2D polynomial transformation function (fitgeotrans function in Matlab). Later, the localizations of single NR molecules with high precision (<20 nm) in each channel were also used as control points to further refine the registration map for each FOV.

Fourth, to compensate for optical aberrations, we used images of bright fluorescent beads and a maximum-likelihood estimator to retrieve the pupil phase function, as reported previously. <sup>27,82</sup> In short, optical aberrations were modeled as a phase mask at the pupil, consisting of the sum of Zernike modes. We considered the first 35 Zernike modes, neglecting the piston (flat), tilt (vertical tilt), and tip (horizontal tilt). We calibrated the aberrations of the two polarized channels independently.

Fifth, the offset-subtracted images, registration map, and Zernike coefficients were used as inputs to our bespoke sparsity-promoting maximum-likelihood estimator, RoSE-O, 47,48 using the same analysis protocol in our previous work.<sup>27</sup> The direct output of the estimator is a list of localizations, which includes the 2D location (x, y), orientational second moment  $m = (m_{xx}, m_{yy}, m_{zz}, m_{xy}, m_{xz}, m_{yz})$ , and signal s of each SM. The second moments were further converted to the mean orientation  $\mu$  and wobble angle  $\alpha$  by minimizing (fmincon function in Matlab) the weighted square error between the measured second moments m from RoSE-O and the second moments computed from the current estimate of  $\mu$  and  $\alpha$ . The weighting matrix is a  $6 \times 6$  Fisher information matrix 83 calculated from the basis images of the polarized vortex SMOLM. The raw fluorescence images (Figure S4, top) from the polarized vortex SMOLM match well with images (Figure S4, middle) reconstructed from the measured orientations (Figure S4, bottom), demonstrating the high performance of the polarized vortex SMOLM and the bespoke estimator. Further, RoSE-O's 5D estimates exhibit essentially no correlations in error between position and orientation, thereby demonstrating good robustness to Poisson shot noise (Figure S9).

When SMOLM images were analyzed, the long axis of each fibril was oriented randomly relative to laboratory coordinates. For each region of interest, the long axis of the fibrils was measured by fitting a collection of (x, y) positions, corresponding to NR blinking along each fibril, using a linear model (*fit* function in Matlab). To ensure accuracy and precision, we applied a signal filter  $s \ge 300$  photons before linear fitting. The measured long axis for each fibril was then

used to generate rotation matrices; after planar rotation transformation, the fibril's long axis is aligned along the x direction, and the NR orientations pointing parallel to the fibril's long axis are parallel to u = (1, 0, 0). For clarity and convenience, we refer to the aligned orientation coordinate system using  $u = (u_x, u_y, u_z)$ .

Theoretical Model Linking the Chirality and Periodicity of Supramolecular Helices to SMOLM Orientation Measurements. As shown in Figure 1a, i, a helical ribbon is composed of two helices of identical pitch. Given a left-handed (LH) helix aligned along the  $\alpha$  axis, we may describe it using the parametric equations

$$x(\tau) = \frac{r\tau}{\tan \delta}$$

$$y(\tau) = r \cos \tau$$

$$z(\tau) = -r \sin \tau$$
(1)

where (x, y, z) describes the helical structure in a local coordinate system,  $\tau$  is the helix phase, r is the radius of the helix, and  $\delta \in [0^{\circ}, 90^{\circ}]$  is the backbone tilt angle. The parameters r and  $\delta$  are determined by the geometry of each helix.

Given that NR binds parallel to the backbone of the helix, the orientations of blinking SMs measured by SMOLM are tangent to the helix and are given by

$$u_{x}(\tau) = \frac{x'(\tau)}{\sqrt{x'(\tau)^{2} + y'(\tau)^{2} + z'(\tau)^{2}}} = \cos \delta$$

$$u_{y}(\tau) = \frac{y'(\tau)}{\sqrt{x'(\tau)^{2} + y'(\tau)^{2} + z'(\tau)^{2}}} = -\sin \tau \sin \delta$$

$$u_{z}(\tau) = \frac{z'(\tau)}{\sqrt{x'(\tau)^{2} + y'(\tau)^{2} + z'(\tau)^{2}}} = -\cos \tau \sin \delta$$
(2)

where  $x'(\tau)$  denotes a partial derivative of  $x(\tau)$  with respect to  $\tau$  and  $(u_x, u_y, u_z)$  represent orientation coordinates with  $||u_x, u_y, u_z|| = 1$  (Figure 1a, ii). Notice that  $u_x$  is parallel to the long axis of the fibril. Similarly, a right-handed (RH) helix aligned along the x axis and the associated orientations of dyes transiently binding to it can be described by

$$x(\tau) = \frac{r\tau}{\tan \delta}$$

$$y(\tau) = r \cos \tau$$

$$z(\tau) = r \sin \tau$$
(3)

and

$$u_{x}(\tau) = \frac{x'(\tau)}{\sqrt{x'(\tau)^{2} + y'(\tau)^{2} + z'(\tau)^{2}}} = \cos \delta$$

$$u_{y}(\tau) = \frac{y'(\tau)}{\sqrt{x'(\tau)^{2} + y'(\tau)^{2} + z'(\tau)^{2}}} = -\sin \tau \sin \delta$$

$$u_{z}(\tau) = \frac{z'(\tau)}{\sqrt{x'(\tau)^{2} + y'(\tau)^{2} + z'(\tau)^{2}}} = \cos \tau \sin \delta$$
(4)

From the above equations, we find that the orientation distributions of LH and RH helices look the same if we neglect the connection between  $\tau$  and the spatial coordinates. That is, accumulating the orientations of all bound SMs along at least one helical period corresponds to a single circle in the orientation domain (Figure 1a, ii, and iv).

Interestingly, given sufficient 3D localization precision relative to the radius r and period of a helix, SMOLM has the potential to reveal the chirality and periodicity of a supramolecular helix. For example, when  $\tau \in [\pi, 2\pi]$  for an LH helix (Figure 1a, i), the structure is at its largest height above the coverslip, and the NR orientations from this region lie on the positive  $u_y \geq 0$  semicircle in the  $u_x \geq 0$  orientation

hemisphere (Figure 1a, ii). The opposite trend holds for RH helices (Figure 1a, iii, and iv). Thus, theoretically, if the height information can be measured with high accuracy and precision, then the connection between helix phase  $\tau$ , helix handedness, and NR orientation distribution can be exploited.

Similarly, the periodicity of the helical structure can be extracted from analyzing the 3D positions of NR binding to each helix, or equivalently, the projection of the helix to a sinusoid in 2D given by  $(x(\tau), y(\tau))$  or  $(x(\tau), z(\tau))$  in eqs 1 and 3. For simplicity, the parameter  $\tau$  is omitted in the following statements. By comparing the parametric equations (eqs 1 and 2 or eqs 3 and 4) across the spatial and orientation domains, we find that the helix period is also encoded in position—orientation pairs  $(x, u_y)$  and  $(x, u_z)$ , with identical period to the position-only pairs (x, y) and (x, z). In addition to these pairs, one may combine all position—orientation measurements for a better signal-to-noise ratio and more precise periodicity measurement.

Both chirality and periodicity are currently hidden in SMOLM data by relatively dim NR blinking events, which enable excellent orientation precision (Figure S7 and Table S1) but cause poor localization precision (Figure S3,  $\sim$ 12 nm in xy). Future work can improve localization precision by designing more advanced adaptive imaging systems and utilizing brighter dyes.

**Helical Optimization Algorithm.** To determine the helical structure of the  $\beta$ -sheet assemblies (Figure S5), we first collected the orientation and rotational mobility measurements of each fluorescent probe along each fibril. The locations are aligned into a common coordinate system, with the fibril's long axis oriented along the x axis and  $u_x$  direction, as described above for the convenience of analysis and interpretation.

Second, we measure structure information by fitting the parameter(s) of a specific helix model to a measured orientation distribution (Figure S5a, iii, and iv). This step is formulated as an optimization problem. For a helical bilayer, we solve

$$\begin{split} (\hat{\delta}_{\text{inner}}, \, \hat{\delta}_{\text{outer}}) &= \underset{(\delta_{\text{inner}}, \delta_{\text{outer}}) \in [\delta_{\text{lower}}, \delta_{\text{upper}}]}{\arg \min} \\ &= \sum_{i} \min\{(\delta_{i} - \delta_{\text{inner}})^{2}, \, (\delta_{i} - \delta_{\text{outer}})^{2}\} \end{split} \tag{5}$$

where  $(\hat{\delta}_{inner}, \hat{\delta}_{outer})$  are the resulting estimates of the inner and outer backbone tilt angles, respectively,  $\delta_i$  represents the ith measurement of the backbone tilt angle from a single NR localization, and i is an index over all localizations on a particular fibril. We calculate  $\delta_i$  from  $u_i$  using  $\delta = \cos^{-1} u_x$ . If we assume that there is only one layer, i.e., a helical monolayer, we solve

$$\hat{\delta}_{\text{mono}} = \underset{\delta_{\text{mono}} \in [\delta_{\text{lower}}, \delta_{\text{upper}}]}{\arg \min} \sum_{i} (\delta_{i} - \delta_{\text{mono}})^{2}$$
(6)

To ensure physically realistic measurements, we constrained the optimization problem using  $\delta_{\rm lower}$  and  $\delta_{\rm upper}$  extracted from our SMOLM data. We use morphological erosion (medfilt2 function in Matlab) to filter out isolated data points with either small or large  $\delta$  (Figure S5b and c). Then, we compute values of  $\delta_{\rm lower}$  and  $\delta_{\rm upper}$  such that the annulus in orientation space bounded by  $\delta_{\rm lower}$  and  $\delta_{\rm upper}$  contains all remaining tilt angle measurements  $\delta$ . For KFE8, we set optimization constraints  $\delta_{\rm lower}=29.23^{\circ}$  and  $\delta_{\rm upper}=68.09^{\circ}$ . For A $\beta$ 42, we set  $\delta_{\rm lower}=0^{\circ}$  and  $\delta_{\rm upper}=21.23^{\circ}$ .

For structure quantification using experimental data, we used a compound filter, i.e., signal  $s \geq 500$  photons and wobble cone half-angle  $\alpha \leq 30^\circ$ . When  $\alpha \geq 30^\circ$ , the backbone tilt angle measurement is less accurate and precise. The signal filter ensures the accuracy and precision of the tilt angle measurements, and we use the wobble cone filter to ensure that the geometry of the helical structure is inferred from NR molecules that are not wobbling excessively during a camera frame. Notably, SMs with large wobble freedom still sense the chemical environment near each helix. Thus, these data are preserved for wobble cone analysis (e.g., Figure 2b), which quantifies the NR binding behavior near each fibril.

#### **ASSOCIATED CONTENT**

#### **Data Availability Statement**

Raw data and simulation and analysis software are available via OSF (https://osf.io/9mf2z/) and from the authors upon reasonable request.

# **Supporting Information**

The Supporting Information is available free of charge at https://pubs.acs.org/doi/10.1021/acsnano.3c11771.

Additional data analysis and simulation studies (Figures S1–S15, Table S1) (PDF)

Example raw TAB SMOLM images collected by the vortex microscope (MP4)

#### **AUTHOR INFORMATION**

#### **Corresponding Author**

Matthew D. Lew — Preston M. Green Department of Electrical and Systems Engineering, McKelvey School of Engineering, Washington University in St. Louis, St. Louis, Missouri 63130, United States; Occid.org/0000-0002-5614-3292; Email: mdlew@wustl.edu

#### **Authors**

Weiyan Zhou — Preston M. Green Department of Electrical and Systems Engineering, McKelvey School of Engineering, Washington University in St. Louis, St. Louis, Missouri 63130, United States; Occid.org/0000-0002-5995-4728

Conor L. O'Neill — Department of Biomedical Engineering, McKelvey School of Engineering, Washington University in St. Louis, St. Louis, Missouri 63130, United States; orcid.org/0000-0003-0714-8828

Tianben Ding — Preston M. Green Department of Electrical and Systems Engineering, McKelvey School of Engineering, Washington University in St. Louis, St. Louis, Missouri 63130, United States; Occid.org/0000-0003-0710-2344

Oumeng Zhang — Preston M. Green Department of Electrical and Systems Engineering, McKelvey School of Engineering, Washington University in St. Louis, St. Louis, Missouri 63130, United States; orcid.org/0000-0001-7318-2130

Jai S. Rudra — Department of Biomedical Engineering, McKelvey School of Engineering, Washington University in St. Louis, St. Louis, Missouri 63130, United States; orcid.org/0000-0002-7837-4980

Complete contact information is available at: https://pubs.acs.org/10.1021/acsnano.3c11771

## **Author Contributions**

W.Z. performed research and analyzed data; W.Z. and C.L.O. prepared samples; T.D. and O.Z. contributed imaging and analytic tools; W.Z., C.L.O., J.S.R., and M.D.L. designed the research; J.S.R. and M.D.L. supervised the research; W.Z., J.S.R., and M.D.L. wrote the paper with input from all authors.

## **Funding**

This work was supported by the National Science Foundation under award number 2047517 to J.S.R. and by the National Institute of General Medical Sciences of the National Institutes of Health under grant number R35GM124858 to M.D.L.

#### **Notes**

The authors declare no competing financial interest. A preprint of this article is available via bioRxiv: Zhou, W.; O'Neill, C. L.; Ding, T.; Zhang, O.; Rudra, J. S.; Lew, M. D. Resolving the nanoscale structure of  $\beta$ -sheet assemblies using

single-molecule orientation-localization microscopy. bioRxiv 2023.09.13.557571. 10.1101/2023.09.13.557571 (accessed September 14, 2023).

#### **ACKNOWLEDGMENTS**

The authors thank T. Wu for inspiring discussions and helpful comments.

### **REFERENCES**

- (1) Liu, R.; Hudalla, G. A. Using Self-Assembling Peptides to Integrate Biomolecules into Functional Supramolecular Biomaterials. *Molecules* **2019**, 24, 1450.
- (2) Li, J.; Zhang, F. Amyloids as Building Blocks for Macroscopic Functional Materials: Designs, Applications and Challenges. *International Journal of Molecular Sciences* **2021**, 22, 10698.
- (3) Bertouille, J.; Kasas, S.; Martin, C.; Hennecke, U.; Ballet, S.; Willaert, R. G. Fast Self-Assembly Dynamics of a  $\beta$ -Sheet Peptide Soft Material. *Small* **2023**, *19*, No. 2206795.
- (4) Weeks, W. B.; Buchanan, L. E. Label-Free Detection of  $\beta$ -Sheet Polymorphism. *J. Phys. Chem. Lett.* **2022**, *13*, 9534–9538.
- (5) Wang, F.; Gnewou, O.; Wang, S.; Osinski, T.; Zuo, X.; Egelman, E. H.; Conticello, V. P. Deterministic Chaos in the Self-Assembly of  $\beta$  Sheet Nanotubes from an Amphipathic Oligopeptide. *Matter* **2021**, *4*, 3217–3231.
- (6) Marini, D. M.; Hwang, W.; Lauffenburger, D. A.; Zhang, S.; Kamm, R. D. Left-Handed Helical Ribbon Intermediates in the Self-Assembly of a  $\beta$ -Sheet Peptide. *Nano Lett.* **2002**, *2*, 295–299.
- (7) Bowerman, C. J.; Nilsson, B. L. Review Self-Assembly of Amphipathic  $\beta$ -Sheet Peptides: Insights and Applications. *Peptide Science* **2012**, *98*, 169–184.
- (8) Iadanza, M. G.; Jackson, M. P.; Hewitt, E. W.; Ranson, N. A.; Radford, S. E. A New Era for Understanding Amyloid Structures and Disease. *Nat. Rev. Mol. Cell Biol.* **2018**, *19*, 755–773.
- (9) Balasco, N.; Diaferia, C.; Morelli, G.; Vitagliano, L.; Accardo, A. Amyloid-Like Aggregation in Diseases and Biomaterials: Osmosis of Structural Information. *Frontiers in Bioengineering and Biotechnology* **2021**, *9*, DOI: 10.3389/fbioe.2021.641372.
- (10) Jalali, S.; Yang, Y.; Mahmoudinobar, F.; Singh, S. M.; Nilsson, B. L.; Dias, C. Using All-Atom Simulations in Explicit Solvent to Study Aggregation of Amphipathic Peptides into Amyloid-like Fibrils. *J. Mol. Liq.* **2022**, *347*, No. 118283.
- (11) Cendrowska, U.; Silva, P. J.; Ait-Bouziad, N.; Müller, M.; Guven, Z. P.; Vieweg, S.; Chiki, A.; Radamaker, L.; Kumar, S. T.; Fändrich, M.; Tavanti, F.; Menziani, M. C.; Alexander-Katz, A.; Stellacci, F.; Lashuel, H. A. Unraveling the Complexity of Amyloid Polymorphism Using Gold Nanoparticles and Cryo-EM. *Proc. Natl. Acad. Sci. U. S. A.* **2020**, *117*, 6866–6874.
- (12) Raskatov, J. A.; Foley, A. R.; Louis, J. M.; Yau, W.-M.; Tycko, R. Constraints on the Structure of Fibrils Formed by a Racemic Mixture of Amyloid- $\beta$  Peptides from Solid-State NMR, Electron Microscopy, and Theory. J. Am. Chem. Soc. **2021**, 143, 13299–13313.
- (13) Miller, J. G.; Hughes, S. A.; Modlin, C.; Conticello, V. P. Structures of Synthetic Helical Filaments and Tubes Based on Peptide and Peptido-Mimetic Polymers. *Q. Rev. Biophys.* **2022**, *55*, No. e2.
- (14) Eanes, E. D.; Glenner, G. G. X-Ray Diffraction Studies on Amyloid Filaments. J. Histochem Cytochem. 1968, 16, 673-677.
- (15) Bücker, R.; Seuring, C.; Cazey, C.; Veith, K.; García-Alai, M.; Grünewald, K.; Landau, M. The Cryo-EM Structures of Two Amphibian Antimicrobial Cross- $\beta$  Amyloid Fibrils. *Nat. Commun.* **2022**, *13* (1), 4356.
- (16) Toyama, B. H.; Weissman, J. S. Amyloid Structure: Conformational Diversity and Consequences. *Annu. Rev. Biochem.* **2011**, *80*, 557–585.
- (17) Cox, H.; Georgiades, P.; Xu, H.; Waigh, T. A.; Lu, J. R. Self-Assembly of Mesoscopic Peptide Surfactant Fibrils Investigated by STORM Super-Resolution Fluorescence Microscopy. *Biomacromolecules* **2017**, *18*, 3481–3491.

- (18) Valades Cruz, C. A.; Shaban, H. A.; Kress, A.; Bertaux, N.; Monneret, S.; Mavrakis, M.; Savatier, J.; Brasselet, S. Quantitative Nanoscale Imaging of Orientational Order in Biological Filaments by Polarized Superresolution Microscopy. *Proc. Natl. Acad. Sci. U. S. A.* **2016**, *113*, E820–E828.
- (19) Rimoli, C. V.; Valades-Cruz, C. A.; Curcio, V.; Mavrakis, M.; Brasselet, S. 4polar-STORM Polarized Super-Resolution Imaging of Actin Filament Organization in Cells. *Nat. Commun.* **2022**, *13*, 301.
- (20) Albertazzi, L.; van der Zwaag, D.; Leenders, C. M. A.; Fitzner, R.; van der Hofstad, R. W.; Meijer, E. W. Probing Exchange Pathways in One-Dimensional Aggregates with Super-Resolution Microscopy. *Science* **2014**, *344*, 491–495.
- (21) Beun, L. H.; Albertazzi, L.; van der Zwaag, D.; de Vries, R.; Cohen Stuart, M. A. Unidirectional Living Growth of Self-Assembled Protein Nanofibrils Revealed by Super-Resolution Microscopy. *ACS Nano* **2016**, *10*, 4973–4980.
- (22) da Silva, R. M. P.; van der Zwaag, D.; Albertazzi, L.; Lee, S. S.; Meijer, E. W.; Stupp, S. I. Super-Resolution Microscopy Reveals Structural Diversity in Molecular Exchange among Peptide Amphiphile Nanofibres. *Nat. Commun.* **2016**, *7*, No. 11561.
- (23) Tholen, M.; Tas, R.; Wang, Y.; Albertazzi, L. Beyond DNA: New Probes for PAINT Super-Resolution Microscopy. *Chem. Commun.* **2023**, *59*, 8332–8342.
- (24) Spehar, K.; Ding, T.; Sun, Y.; Kedia, N.; Lu, J.; Nahass, G. R.; Lew, M. D.; Bieschke, J. Super-Resolution Imaging of Amyloid Structures over Extended Times by Using Transient Binding of Single Thioflavin T Molecules. *ChemBioChem.* **2018**, *19*, 1944–1948.
- (25) Ries, J.; Udayar, V.; Soragni, A.; Hornemann, S.; Nilsson, K. P. R.; Riek, R.; Hock, C.; Ewers, H.; Aguzzi, A. A.; Rajendran, L. Superresolution Imaging of Amyloid Fibrils with Binding-Activated Probes. *ACS Chem. Neurosci.* **2013**, *4*, 1057–1061.
- (26) Ding, T.; Wu, T.; Mazidi, H.; Zhang, O.; Lew, M. D. Single-Molecule Orientation Localization Microscopy for Resolving Structural Heterogeneities between Amyloid Fibrils. *Optica* **2020**, *7*, 602.
- (27) Ding, T.; Lew, M. D. Single-Molecule Localization Microscopy of 3D Orientation and Anisotropic Wobble Using a Polarized Vortex Point Spread Function. *J. Phys. Chem. B* **2021**, *125*, 12718–12729.
- (28) Bongiovanni, M. N.; Godet, J.; Horrocks, M. H.; Tosatto, L.; Carr, A. R.; Wirthensohn, D. C.; Ranasinghe, R. T.; Lee, J.-E.; Ponjavic, A.; Fritz, J. V.; Dobson, C. M.; Klenerman, D.; Lee, S. F. Multi-Dimensional Super-Resolution Imaging Enables Surface Hydrophobicity Mapping. *Nat. Commun.* **2016**, *7*, No. 13544.
- (29) Needham, L.-M.; Weber, J.; Varela, J. A.; Fyfe, J. W. B.; Do, D. T.; Xu, C. K.; Tutton, L.; Cliffe, R.; Keenlyside, B.; Klenerman, D.; Dobson, C. M.; Hunter, C. A.; Müller, K. H.; O'Holleran, K.; Bohndiek, S. E.; Snaddon, T. N.; Lee, S. F. ThX a next-Generation Probe for the Early Detection of Amyloid Aggregates. *Chem. Sci.* 2020, 11, 4578—4583.
- (30) Sarkar, A.; Namboodiri, V.; Kumbhakar, M. Single-Molecule Orientation Imaging Reveals Two Distinct Binding Configurations on Amyloid Fibrils. *J. Phys. Chem. Lett.* **2023**, *14*, 4990–4996.
- (31) Lee, J.-E.; Sang, J. C.; Rodrigues, M.; Carr, A. R.; Horrocks, M. H.; De, S.; Bongiovanni, M. N.; Flagmeier, P.; Dobson, C. M.; Wales, D. J.; Lee, S. F.; Klenerman, D. Mapping Surface Hydrophobicity of  $\alpha$ -Synuclein Oligomers at the Nanoscale. *Nano Lett.* **2018**, *18*, 7494–7501.
- (32) Backlund, M. P.; Lew, M. D.; Backer, A. S.; Sahl, S. J.; Moerner, W. E. The Role of Molecular Dipole Orientation in Single-Molecule Fluorescence Microscopy and Implications for Super-Resolution Imaging. *ChemPhysChem* **2014**, *15*, 587–599.
- (33) Zhang, O.; Guo, Z.; He, Y.; Wu, T.; Vahey, M. D.; Lew, M. D. Six-Dimensional Single-Molecule Imaging with Isotropic Resolution Using a Multi-View Reflector Microscope. *Nat. Photonics* **2023**, *17*, 179–186.
- (34) Wu, T.; Lu, J.; Lew, M. D. Dipole-Spread-Function Engineering for Simultaneously Measuring the 3D Orientations and 3D Positions of Fluorescent Molecules. *Optica* **2022**, *9*, 505–511.

- (35) Klymchenko, A. S. Solvatochromic and Fluorogenic Dyes as Environment-Sensitive Probes: Design and Biological Applications. *Acc. Chem. Res.* **2017**, *50*, 366–375.
- (36) Kurniasih, I. N.; Liang, H.; Mohr, P. C.; Khot, G.; Rabe, J. P.; Mohr, A. Nile Red Dye in Aqueous Surfactant and Micellar Solution. *Langmuir* **2015**, *31*, 2639–2648.
- (37) Ding, T.; Spehar, K.; Bieschke, J.; Lew, M. D. Long-Term, Super-Resolution Imaging of Amyloid Structures Using Transient Amyloid Binding Microscopy. In *Single Molecule Spectroscopy and Superresolution Imaging XII*; Gregor, I., Gryczynski, Z. K., Koberling, F., Eds.; SPIE: San Francisco, CA, USA, 2019; p 19.
- (38) Clover, T. M.; O'Neill, C. L.; Appavu, R.; Lokhande, G.; Gaharwar, A. K.; Posey, A. E.; White, M. A.; Rudra, J. S. Self-Assembly of Block Heterochiral Peptides into Helical Tapes. *J. Am. Chem. Soc.* **2020**, *142*, 19809–19813.
- (39) Schmidt, M.; Rohou, A.; Lasker, K.; Yadav, J. K.; Schiene-Fischer, C.; Fändrich, M.; Grigorieff, N. Peptide Dimer Structure in an  $A\beta(1-42)$  Fibril Visualized with Cryo-EM. *Proc. Natl. Acad. Sci. U. S. A.* **2015**, *112*, 11858–11863.
- (40) Lee, M.; Yau, W.-M.; Louis, J. M.; Tycko, R. Structures of Brain-Derived 42-Residue Amyloid- $\beta$  Fibril Polymorphs with Unusual Molecular Conformations and Intermolecular Interactions. *Proc. Natl. Acad. Sci. U. S. A.* **2023**, 120, No. e2218831120.
- (41) Watanabe-Nakayama, T.; Ono, K.; Itami, M.; Takahashi, R.; Teplow, D. B.; Yamada, M. High-Speed Atomic Force Microscopy Reveals Structural Dynamics of Amyloid B1–42 Aggregates. *Proc. Natl. Acad. Sci. U. S. A.* **2016**, *113*, 5835–5840.
- (42) Varela, J. A.; Rodrigues, M.; De, S.; Flagmeier, P.; Gandhi, S.; Dobson, C. M.; Klenerman, D.; Lee, S. F. Optical Structural Analysis of Individual  $\alpha$ -Synuclein Oligomers. *Angew. Chem., Int. Ed.* **2018**, *57*, 4886–4890.
- (43) Wu, T.; Lu, P.; Rahman, M. A.; Li, X.; Lew, M. D. Deep-SMOLM: Deep Learning Resolves the 3D Orientations and 2D Positions of Overlapping Single Molecules with Optimal Nanoscale Resolution. *Opt. Express* **2022**, *30*, 36761–36773.
- (44) Wu, C.; Wang, Z.; Lei, H.; Zhang, W.; Duan, Y. Dual Binding Modes of Congo Red to Amyloid Protofibril Surface Observed in Molecular Dynamics Simulations. *J. Am. Chem. Soc.* **2007**, *129*, 1225–1232
- (45) Biancalana, M.; Koide, S. Molecular Mechanism of Thioflavin-T Binding to Amyloid Fibrils. *Biochimica et Biophysica Acta (BBA) Proteins and Proteomics* **2010**, *1804*, 1405–1412.
- (46) Skeby, K. K.; Sørensen, J.; Schiøtt, B. Identification of a Common Binding Mode for Imaging Agents to Amyloid Fibrils from Molecular Dynamics Simulations. *J. Am. Chem. Soc.* **2013**, *135*, 15114–15128.
- (47) Mazidi, H.; King, E. S.; Zhang, O.; Nehorai, A.; Lew, M. D. Dense Super-Resolution Imaging of Molecular Orientation Via Joint Sparse Basis Deconvolution and Spatial Pooling. 2019 IEEE 16th International Symposium on Biomedical Imaging (ISBI 2019); IEEE, 2019; pp 325–329.
- (48) Mazidi, H.; Ding, T.; Lew, M. RoSE-O (Robust Statistical Estimation Algorithm for Single-Molecule Orientation Measurement); GitHub: https://github.com/Lew-Lab/RoSE-O, 2020.
- (49) Gremer, L.; Schölzel, D.; Schenk, C.; Reinartz, E.; Labahn, J.; Ravelli, R. B. G.; Tusche, M.; Lopez-Iglesias, C.; Hoyer, W.; Heise, H.; Willbold, D.; Schröder, G. F. Fibril Structure of Amyloid- $\beta$ (1–42) by Cryo–Electron Microscopy. *Science* **2017**, *358*, 116–119.
- (50) Shaban, H. A.; Valades-Cruz, C. A.; Savatier, J.; Brasselet, S. Polarized Super-Resolution Structural Imaging inside Amyloid Fibrils Using Thioflavine T. *Sci. Rep.* **2017**, *7*, No. 12482.
- (51) Hwang, W.; Marini, D. M.; Kamm, R. D.; Zhang, S. Supramolecular Structure of Helical Ribbons Self-Assembled from a β-Sheet Peptide. *I. Chem. Phys.* **2003**, *118*, 389–397.
- (52) Lee, N. R.; Bowerman, C. J.; Nilsson, B. L. Effects of Varied Sequence Pattern on the Self-Assembly of Amphipathic Peptides. *Biomacromolecules* **2013**, *14*, 3267–3277.

- (53) Weeks, W. B.; Tainter, C. J.; Buchanan, L. E. Investigating the Effects of N-Terminal Acetylation on KFE8 Self-Assembly with 2D IR Spectroscopy. *Biophys. J.* **2022**, *121*, 1549–1559.
- (54) Backer, A. S.; Moerner, W. E. Extending Single-Molecule Microscopy Using Optical Fourier Processing. *J. Phys. Chem. B* **2014**, *118*, 8313–8329.
- (55) Lattanzi, V.; André, I.; Gasser, U.; Dubackic, M.; Olsson, U.; Linse, S. Amyloid  $\beta$  42 Fibril Structure Based on Small-Angle Scattering. *Proc. Natl. Acad. Sci. U. S. A.* **2021**, *118*, No. e2112783118.
- (56) Gray, V. P.; Amelung, C. D.; Duti, I. J.; Laudermilch, E. G.; Letteri, R. A.; Lampe, K. J. Biomaterials via Peptide Assembly: Design, Characterization, and Application in Tissue Engineering. *Acta Biomaterialia* **2022**, *140*, 43–75.
- (57) Acar, H.; Srivastava, S.; Chung, E. J.; Schnorenberg, M. R.; Barrett, J. C.; LaBelle, J. L.; Tirrell, M. Self-Assembling Peptide-Based Building Blocks in Medical Applications. *Adv. Drug Delivery Rev.* **2017**, *110*–111, 65–79.
- (58) Wang, Q.; Zhang, X.; Zheng, J.; Liu, D. Self-Assembled Peptide Nanotubes as Potential Nanocarriers for Drug Delivery. *RSC Adv.* **2014**, *4*, 25461–25469.
- (59) Ivnitski, D.; Amit, M.; Silberbush, O.; Atsmon-Raz, Y.; Nanda, J.; Cohen-Luria, R.; Miller, Y.; Ashkenasy, G.; Ashkenasy, N. The Strong Influence of Structure Polymorphism on the Conductivity of Peptide Fibrils. *Angew. Chem., Int. Ed.* **2016**, *55*, 9988–9992.
- (60) Buchanan, L. E.; Maj, M.; Dunkelberger, E. B.; Cheng, P.-N.; Nowick, J. S.; Zanni, M. T. Structural Polymorphs Suggest Competing Pathways for the Formation of Amyloid Fibrils That Diverge from a Common Intermediate Species. *Biochemistry* **2018**, *57*, 6470–6478.
- (61) Wei, G.; Su, Z.; Reynolds, N. P.; Arosio, P.; Hamley, I. W.; Gazit, E.; Mezzenga, R. Self-Assembling Peptide and Protein Amyloids: From Structure to Tailored Function in Nanotechnology. *Chem. Soc. Rev.* **2017**, *46*, 4661–4708.
- (62) Tenidis, K.; Waldner, M.; Bernhagen, J.; Fischle, W.; Bergmann, M.; Weber, M.; Merkle, M.-L.; Voelter, W.; Brunner, H.; Kapurniotu, A. Identification of a Penta- and Hexapeptide of Islet Amyloid Polypeptide (IAPP) with Amyloidogenic and Cytotoxic Properties 1 Edited by R. Huber. J. Mol. Biol. 2000, 295, 1055–1071.
- (63) Kazantzis, A.; Waldner, M.; Taylor, J. W.; Kapurniotu, A. Conformationally Constrained Human Calcitonin (hCt) Analogues Reveal a Critical Role of Sequence 17–21 for the Oligomerization State and Bioactivity of hCt. Eur. J. Biochem. 2002, 269, 780–791.
- (64) Zheng, J.; Ma, B.; Tsai, C.-J.; Nussinov, R. Structural Stability and Dynamics of an Amyloid-Forming Peptide GNNQQNY from the Yeast Prion Sup-35. *Biophys. J.* **2006**, *91*, 824–833.
- (65) Hilbich, C.; Kisters-Woike, B.; Reed, J.; Masters, C. L.; Beyreuther, K. Substitutions of Hydrophobic Amino Acids Reduce the Amyloidogenicity of Alzheimer's Disease  $\beta$ A4 Peptides. *J. Mol. Biol.* **1992**, 228, 460–473.
- (66) Zhang, S. Self-Assembling Peptides: From a Discovery in a Yeast Protein to Diverse Uses and Beyond. *Protein Sci.* **2020**, 29, 2281–2303.
- (67) Karavasili, C.; Fatouros, D. G. Self-Assembling Peptides as Vectors for Local Drug Delivery and Tissue Engineering Applications. *Adv. Drug Delivery Rev.* **2021**, *174*, 387–405.
- (68) Colletier, J.-P.; Laganowsky, A.; Landau, M.; Zhao, M.; Soriaga, A. B.; Goldschmidt, L.; Flot, D.; Cascio, D.; Sawaya, M. R.; Eisenberg, D. Molecular Basis for Amyloid- $\beta$  Polymorphism. *Proc. Natl. Acad. Sci. U. S. A.* **2011**, *108*, 16938–16943.
- (69) Mehra, S.; Gadhe, L.; Bera, R.; Sawner, A. S.; Maji, S. K. Structural and Functional Insights into  $\alpha$ -Synuclein Fibril Polymorphism. *Biomolecules* **2021**, *11*, 1419.
- (70) Qiang, W.; Yau, W.-M.; Lu, J.-X.; Collinge, J.; Tycko, R. Structural Variation in Amyloid-β Fibrils from Alzheimer's Disease Clinical Subtypes. *Nature* **2017**, 541, 217–221.
- (71) Paravastu, A. K.; Leapman, R. D.; Yau, W.-M.; Tycko, R. Molecular Structural Basis for Polymorphism in Alzheimer's  $\beta$ -Amyloid Fibrils. *Proc. Natl. Acad. Sci. U. S. A.* **2008**, *105*, 18349—18354.

- (72) Gremer, L.; Schölzel, D.; Schenk, C.; Reinartz, E.; Labahn, J.; Ravelli, R. B. G.; Tusche, M.; Lopez-Iglesias, C.; Hoyer, W.; Heise, H.; Willbold, D.; Schröder, G. F. Fibril Structure of Amyloid- $\beta$ (1–42) by Cryo–Electron Microscopy. *Science* **2017**, 358, 116–119.
- (73) Colvin, M. T.; Silvers, R.; Ni, Q. Z.; Can, T. V.; Sergeyev, I.; Rosay, M.; Donovan, K. J.; Michael, B.; Wall, J.; Linse, S.; Griffin, R. G. Atomic Resolution Structure of Monomorphic  $A\beta$ 42 Amyloid Fibrils. *J. Am. Chem. Soc.* **2016**, *138*, 9663–9674.
- (74) Wälti, M. A.; Ravotti, F.; Arai, H.; Glabe, C. G.; Wall, J. S.; Böckmann, A.; Güntert, P.; Meier, B. H.; Riek, R. Atomic-Resolution Structure of a Disease-Relevant  $A\beta(1-42)$  Amyloid Fibril. *Proc. Natl. Acad. Sci. U. S. A.* **2016**, *113*, E4976–E4984.
- (75) Reinhardt, S. C. M.; Masullo, L. A.; Baudrexel, I.; Steen, P. R.; Kowalewski, R.; Eklund, A. S.; Strauss, S.; Unterauer, E. M.; Schlichthaerle, T.; Strauss, M. T.; Klein, C.; Jungmann, R. Ångström-Resolution Fluorescence Microscopy. *Nature* **2023**, *617*, 711–716.
- (76) Weber, M.; von der Emde, H.; Leutenegger, M.; Gunkel, P.; Sambandan, S.; Khan, T. A.; Keller-Findeisen, J.; Cordes, V. C.; Hell, S. W. MINSTED Nanoscopy Enters the Ångström Localization Range. *Nat. Biotechnol.* **2023**, *41*, 569–576.
- (77) O'Neill, C. L.; Shrimali, P. C.; Clapacs, Z. P.; Files, M. A.; Rudra, J. S. Peptide-Based Supramolecular Vaccine Systems. *Acta Biomaterialia* **2021**, *133*, 153–167.
- (78) Files, M. A.; Kristjansson, K. M.; Rudra, J. S.; Endsley, J. J. Nanomaterials-Based Vaccines to Target Intracellular Bacterial Pathogens. *Frontiers in Microbiology* **2022**, *13*, DOI: 10.3389/fmicb.2022.1040105.
- (79) Bowerman, C. J.; Ryan, D. M.; Nissan, D. A.; Nilsson, B. L. The Effect of Increasing Hydrophobicity on the Self-Assembly of Amphipathic β-Sheet Peptides. *Mol. BioSyst.* **2009**, *5*, 1058–1069.
- (80) Ovesný, M.; Křížek, P.; Borkovec, J.; Švindrych, Z.; Hagen, G. M. ThunderSTORM: A Comprehensive ImageJ Plug-in for PALM and STORM Data Analysis and Super-Resolution Imaging. *Bioinformatics* **2014**, *30*, 2389–2390.
- (81) Schneider, C. A.; Rasband, W. S.; Eliceiri, K. W. NIH Image to ImageJ: 25 Years of Image Analysis. *Nat. Methods* **2012**, *9*, 671–675.
- (82) Mazidi, H.; Ding, T.; Nehorai, A.; Lew, M. D. Quantifying Accuracy and Heterogeneity in Single-Molecule Super-Resolution Microscopy. *Nat. Commun.* **2020**, *11*, 6353.
- (83) Kay, S. Fundamentals of Statistical Signal Processing, Vol. I: Estimation Theory, 1st ed.; Pearson: Englewood Cliffs, NJ, USA, 1993.